Pre-print

Resentini R., Malusà M.G., Garzanti E. (2020) Ongoing exhumation of the Taiwan orogenic wedge revealed by detrital apatite thermochronology: The impact of effective mineral fertility and zero-track grains. *Earth and Planetary Science Letters* 544, 116374, 1-13

https://doi.org/10.1016/j.epsl.2020.116374

Ongoing exhumation of the Taiwan orogenic wedge revealed by detrital apatite thermochronology: the impact of effective mineral fertility and zero-track grains

Alberto Resentini, Marco G. Malusà*, Eduardo Garzanti

Laboratory for Provenance Studies, Department of Earth and Environmental Sciences, University of Milano-Bicocca, Milano 20126, Italy

* Corresponding author: marco.malusa@unimib.it

Abstract

In clastic detritus derived from the erosion of young active orogens, the geologic interpretation of apatite fission-track (AFT) data is hampered by the occurrence of grains without spontaneous tracks and by contributions from multiple eroding sources with different apatite fertilities. Here, we use the Taiwan orogen as a test case to illustrate how to overcome these problems and deal with zero-track grains in detrital AFT studies following long-established principles of fission-track statistics. Our results support the effectiveness of Raman spectroscopy for a reliable identification of apatite grains. We found that zero-track grains are dominant in Taiwan modern sands, and generally contain enough U to provide useful AFT age constraints to exhumation. The absence of spontaneous tracks in most of these grains is due to a short residence time below the temperature of total AFT annealing rather than to low U concentration. Detrital AFT data shows that the extent of the Taiwan AFT reset zone previously inferred from bedrock data was partly underestimated. The revised AFT reset zone includes the southernmost part of the island and, when combined with published ZFT data, supports a scenario of southward progressing exhumation during arc-continent collision. The application of the Taiwan lesson to clastic detritus derived from the

Himalaya resolves paradoxical interpretations of detrital fission-track data sets recently published in the framework of IODP Expedition 354, pointing to a major role of the Namche Barwa syntaxis as a source of apatite grains shed to the Bengal Fan.

Keywords: detrital apatite; fission-track thermochronology; zero-track grains; effective mineral fertility; Taiwan; Bengal Fan.

1. Introduction

Low-temperature thermochronological methods such as apatite fission-track (AFT) thermochronology (Wagner and van den Haute 1992) provide crucial information to constrain the exhumation history of orogenic belts. In young active accretionary prisms largely consisting of low-grade metamorphic rocks, the use of AFT thermochronology is commonly hampered by the occurrence of apatite grains with low U concentration [U] yielding few spontaneous fission tracks, if any (e.g., Kirstein et al. 2010; Baldwin et al. 2019). Data obtained from only a few fission tracks in sporadic apatite crystals are affected by large analytical errors (e.g., Galbraith 2005) and may thus lead to poorly constrained geological interpretations, especially when a conspicuous population of apatite grains lacking spontaneous tracks is not properly accounted for. These problems become even more evident when AFT thermochronology is applied to sediment samples derived from multiple eroding sources, and markedly different fertilities of parent rocks come into play (Malusà et al. 2017). A recent detrital AFT data set for the Bengal Fan (Huyghe et al. 2020), fed from the rapidly exhuming Namche Barwa syntaxis and from other regions of the central-eastern Himalaya eroded at slower rates (e.g., Garzanti 2019), includes many zero-track grains possibly derived from a rapidly exhuming syntaxial source (e.g., Najman et al. 2019). However, information provided by zero-track grains was partly dismissed, and that signal was not detected by Huyghe et al. (2020). An approach to overcome these problems based on recommendations

by Galbraith (2005) is illustrated in this article using the Taiwan orogen as a test case. Based on results from Taiwan, we provide an improved interpretation for the Bengal Fan data set, which is fully consistent with geologic constraints available for the Himalayan region.

2. Fission-track characteristics of apatite grains

Fission-track dating is based on the analysis of tracks, revealed by chemical etching, that accumulate over time in the crystal lattice because of natural, spontaneous fission of ^{238}U atoms (Wagner and van den Haute 1992). According to the External Detector Method (EDM), etched apatite grains are irradiated in a nuclear reactor to determine their [U], based on the density of fission tracks induced by each grain on a muscovite external detector. Both spontaneous and induced track densities are required to obtain a fission-track age, reflecting the time elapsed since the first track retention, and to attempt a geologic interpretation of that age (e.g., Reiner and Ehlers 2006; Malusà and Fitzgerald 2019). Some apatite grains in a sediment sample may not show spontaneous fission tracks, either because the residence time below the temperature of total annealing was too short, or because the [U] is too low. The occurrence of zero-track grains makes the geologic interpretation of AFT data sets challenging (Bardsley 1983; Galbraith 2005). Zero-track grains with very low [U] may even fail to induce tracks in the external detector (U-poor zero-track grains in Fig. 1A), whereas zero-track grains with higher [U] do induce tracks in the external detector (U-rich zero-track grains in Fig. 1A), and the lack of spontaneous tracks in those grains is mainly due to a short residence time below the temperature of total annealing (Galbraith 2005).

A source of detritus may either shed U-poor zero-track grains, U-rich zero-track grains, or grains with fission tracks, all of them contributing to the total apatite fertility of that source (Fig. 1B). The total apatite fertility can be directly quantified by the application of appropriate separation procedures to sediment samples not significantly affected by

79 hydraulic-sorting processes (Malusà et al. 2016). However, the relative abundance of
80 different apatite types may vary considerably depending on the geologic evolution of each
81 source. For example, low-grade metamorphic rocks are expected to shed many apatite grains
82 with low [U] because of cogenetic epidote/allanite and/or monazite growth (Harlov 2015;
83 O'Sullivan et al. 2020). Apatite grains in Bengal Fan sediments (Huyghe et al. 2020) yield
84 ratios of U-rich zero-track grains vs. grains with fission tracks around ~1/3 (Fig. 1C). U-poor
85 zero-track grains are obviously not datable by the AFT method. U-rich zero-track grains,
86 however, do provide useful age constraints that should complement information provided by
87 grains with fission tracks. In detrital AFT studies, the effective apatite fertility, first
88 introduced here to indicate the concentration of datable U-rich zero-track grains and grains
89 with fission tracks (Fig. 1B), is even more important than the total apatite fertility, and its
90 impact should be carefully considered during data interpretation.

91 For zero-track grains, standard fission-track equations formally yield age estimates of
92 zero with infinite relative standard errors that are neither useful nor appropriate. In that case,
93 precision is better indicated by calculating a confidence interval (see Galbraith 2005, his sect.
94 3.11), an approach that should be followed for any grains including few spontaneous tracks.
95 U-rich zero-track grains potentially encompass the entire age range between 0 Ma (minimum-
96 age scenario) and the age corresponding to a single spontaneous track for the measured [U]
97 concentration (maximum-age scenario). This age range and the associated confidence interval
98 get progressively narrower for increasing [U], becoming as narrow as a few Ma and thus
99 geologically significant for [U] > 10 ppm (Fig. 1A,C). An accurate detection and
100 characterization of zero-track grains relative to grains with fission tracks is particularly
101 important in young active orogens. Grains with fission tracks are easily detected in a grain
102 mount, whereas zero-track grains can be revealed by inspecting not only the grain mount, but
103 also the distributions of induced tracks that reproduce the grain shapes in the external

104 detector. However, U-bearing minerals other than apatite can induce fission tracks in the
105 external detector, and the detection of zero-track grains only based on inspection of induced
106 tracks may be difficult when induced track densities are low. Raman spectroscopy provides a
107 suitable tool for a systematic identification of all apatite grains in a detrital sample (Fig. 1D),
108 providing a reliable starting point to quantify the relative proportions of apatite grains with
109 different fission-track characteristics.

110 **3. Geological setting**

111 The island of Taiwan was formed by subduction of the Chinese passive continental
112 margin beneath the Philippine Sea plate and progressive collision with the Luzon magmatic
113 arc (Fig. 2A), which initiated ~6.5 Ma ago and continues with a convergence rate of ~80
114 mm/a (Suppe 1981; 1984; Byrne et al. 2011). The doubly-vergent Taiwan orogen is a stack of
115 tectonic units showing eastward increasing metamorphic grade and unroofing depths,
116 juxtaposed along the Longitudinal Fault against relicts of the Luzon Arc (Fig. 2B).

117 The Western Foothills consist of Neogene shallow-marine sediments originally
118 deposited along the Chinese passive margin, passing westward to virtually undeformed
119 alluvial deposits of the Coastal Plain (Mouthereau et al. 2002). The Slate Belt includes an
120 Eocene to Miocene passive-margin succession that underwent up to lower greenschist-facies
121 metamorphism during arc-continent collision, and the Hsuehshan Range. The latter forms the
122 northwestern outer part of the Slate Belt and comprises Eocene/Oligocene sandstones and
123 shales with a higher degree of graphitization of carbonaceous material (Beyssac et al. 2007).
124 Farther to the east, the Tananao Complex includes the polymetamorphic Tailuko belt that
125 experienced amphibolite-facies metamorphism around 90 Ma (Yui et al. 2012) and an
126 oceanic mélange with exotic blueschist blocks (Yuli Belt; Beyssac et al. 2008). To the east of
127 the suture zone marked by the Longitudinal Fault, the Coastal Range includes Miocene

andesites of the Luzon Arc (Huang et al. 2006) and post-collisional Plio-Pleistocene siliciclastic rocks (Dorsey 1988).

3.1 Previous thermochronologic information

Because of recent rapid exhumation and ongoing mountain building, Taiwan has been the target of low-temperature thermochronologic analyses aimed at constraining the thermal and kinematic evolution of the orogen. Fission-track dating has been applied mostly on zircon, with large datasets covering the entire island that are based on the analysis of modern sand and bedrock from both natural exposures and boreholes (Tsao 1996; Liu et al. 2001; Willett et al. 2003; Lee et al. 2006, 2015; Kirstein et al. 2010, 2014; Mesalles et al. 2014; Hsu et al. 2016; Fellin et al. 2017). Instead, thermochronological data on apatite are sparse because, owing to very fast exhumation rates, apatite seldom shows fission tracks (with exceptions for the Coastal Range, the Western Foothills, and peripheral parts of the Slate Belt; Willett et al. 2003; Fuller et al. 2006; Kirstein et al. 2010).

Across Taiwan, zircon fission-track (ZFT) ages range from 100 Ma to less than 1 Ma. The exhumation of the collisional wedge started around 6 Ma and is generally held to have progressed southward (Suppe, 1981; Willett et al. 2003; Lee et al. 2006). Along the western margin of the island, zircon grains in detritus from the unmetamorphosed Western Foothills yield ZFT ages > 90 Ma (Liu et al. 2001). Along the central and retro-side of the orogen (Slate Belt and Tananao Complex), zircon grains yield totally or partially reset ZFT ages < 10 Ma (Fuller et al. 2006), reflecting the recent exhumation of the axial belt (Fig. 2D). Plio-Pleistocene sandstones of the Coastal Range yield zircons with ZFT ages spanning from 3 Ma to >300 Ma, unreset after deposition (Kirstein et al. 2010). AFT ages depict a similar pattern, with much younger ages (mostly 0-30 Ma; Willett et al. 2003) owing to the lower temperature of the apatite partial-annealing zone above which fission tracks are preserved,

and a wider reset zone that broadly corresponds to the entire metamorphic nappe stack but pinches out at ~22° 30' N (Fig. 2C).

4. Methods

All around Taiwan, 22 modern sand samples were collected for AFT analysis in October 2012 (Fig. 2). We sampled active fluvial bars from both major rivers and minor streams draining single geological domains in order to characterize their apatite fingerprints in terms of both AFT ages and fertility. The studied rivers drain ~20,000 km^2 overall, representing > 50% of the total surface area of Taiwan (36,000 km^2) and all exposed tectonic domains.

A split aliquot of each sample was dry sieved to determine its grain size and sorting, and thus to identify the most suitable size window to maximize apatite recovery (Resentini et al. 2013) and quantify the amount of apatite contained in the finer and coarser tails of the size distribution not considered further for analysis. The rest of the sample was sieved into the selected size window (2-4 ϕ for finer samples and 1-3 ϕ for coarser samples). Denser grains were concentrated by using a Gemeni shaking table and then by centrifuging in Na-polytungstate (ρ = 2.90 g/cm^3). The dense fraction was processed with a Frantz magnetic separator to extract diamagnetic grains, and finally apatite was separated from zircon in liquid diiodomethane (ρ = 3.32 g/cm^3). The resulting material was carefully weighed after each step, also to detect anomalous concentrations of dense minerals potentially caused by hydrodynamic effects. For each sample, the concentration of apatite and zircon grains in the bulk sediment was measured as the ratio between the weight of the mineral separates corrected for spurious grains and the total weight of the processed sediment (procedure illustrated in Malusà and Garzanti 2019).

Apatite grains were prepared for EDM age dating according to the procedure described by Kohn et al. (2019) and etched with 5N HNO_3 at 20˚C for 20 s. Samples were irradiated in

176 the Thermal Column of the Triga reactor at Oregon State University with a nominal dose of
177 ~9×10^{15} n cm^2, using two IRMM-540R standard glasses, one at the top and one at the bottom
178 of each irradiation package to monitor spatial neutron-flux gradients. After irradiation,
179 muscovite detectors were etched with 40% hydrofluoric acid for 45 min. Fission tracks were
180 counted by A.R. at the Laboratory for Provenance Studies (University of Milano-Bicocca)
181 under an optical microscope at 1250× magnification. Because of the young thermal resetting
182 and low [U], many apatite grains yielded no spontaneous fission track. Raman spectroscopy
183 was then used to ensure reliable identification of all apatite grains on grain mounts and
184 determine the proportion, relative to total apatite, of U-poor apatite grains yielding no
185 induced fission track in the external detector. Because matching exactly U-rich apatite grains
186 with their mica image can be difficult if [U] is not sufficiently high, a mosaic image of the
187 mica detector was used to check and refine the coupling of each apatite grain with the
188 corresponding image in the external detector (Fig. 1D).

189 **5. Results**

190 Fertility values and relative proportions of apatite grains with different fission-track
191 characteristics are given in Figs. 2 and 3. The relationships between total fertility and sample
192 grain-size and sorting, as well as heavy-mineral concentrations and bulk grain densities are
193 summarized in Fig. S1. Detrital AFT age distributions are shown in Fig. 4. Confidence
194 intervals for single-grain ages are provided in Fig. 5 (see supplementary material for the full
195 data set). Central ages and number of spontaneous and induced tracks and track densities are
196 summarized in Table 1.

197 ***5.1 Mineral fertilities and fission-track characteristics of apatite grains***

198 The analyzed sediment samples show no apparent relationship between apatite or
199 zircon concentration and textural parameters (Fig. S1). This indicates that potential bias due

200 to selective entrainment is negligible and that the mineral concentration in the sediment can
201 be used to infer the total mineral fertility of the eroded bedrock. The total apatite fertility in
202 Taiwanese catchments spans over three orders of magnitude (Fig 2C). Fertility is extremely
203 low (<10 mg/kg) in catchments draining the Coastal Range, and very low (<50 mg/kg) in
204 catchments draining the Western Foothills, northern and southern parts of the Slate Belt, and
205 Hsuehshan Range. Values are higher (200-300 mg/kg) in the eastern central sector of the
206 island, including the Tananao Complex and the Slate Belt in the upper Zhuoshui catchment,
207 and reach 600 mg/kg in the Xiuguluan catchment. In the same catchments, zircon fertility
208 spans over two orders of magnitude (25 mg/kg on average; Fig 2D), with higher values (~60
209 mg/kg) recorded in the eastern central sector of the island (Tananao Complex). In the
210 northwestern central sector, zircon fertility increases from 30-45 mg/kg in the Dajia and
211 upper Zhuoshui catchment to 100 mg/kg in the upper Da'an and Houlong catchments. The
212 effective apatite fertility in Taiwanese catchments is indicated in Fig. 3, spanning from 0.5
213 mg/kg in rocks exposed in the Xindian catchment to 376.5 mg/kg in rocks exposed in the
214 Xiuguluan catchment.

215 Apatite grains with fission tracks invariably represent the smallest population of the
216 total apatite flux (Fig. 3), with the only exception of samples 18 and 19 (Lehe and Bie Rivers
217 draining volcanic and sedimentary rocks of the Coastal Range). Apatite grains with fission
218 tracks are shed mostly from unreset external units (i.e., Coastal Range and Western
219 Foothills), and locally from recently exhumed metamorphic units (e.g., sample 13 Heping
220 River) (Figs. 3 and 4). U-poor and U-rich zero-track grains represent 0-36% and 0-64%,
221 respectively, of total detrital apatite in Coastal Range samples (S18, S19, S20). In the other
222 samples, U-rich zero-track grains vary from 13% to 75% (~45% on average), and U-poor
223 grains from 25% to 90% (~46% on average). U-rich zero-track grains are widespread in

metamorphic units of the Tananao Complex and the Slate Belt, where they likely reflect recent exhumation above the partial annealing zone.

5.2 Gran-age distributions

The detrital AFT age distributions of Taiwanese samples are illustrated in the radial plots of Fig. 4. In these plots, grains with fission tracks are indicated by full dots. U-rich zero-track grains are indicated by vertical bars encompassing the age range comprised between 0 Ma (minimum-age scenario) and the age corresponding to a single spontaneous track for the measured [U] (maximum-age scenario). The associated 95% confidence intervals are shown in Fig. 5. Most of the samples show unimodal grain age distributions (Fig. 4). Grains with higher [U] (Ni $\geq$ 50 in Fig. 5) generally yield very young AFT ages. In case defects were inadvertently included in spontaneous track counts for some grains, this would imply an overestimation of Ns and even younger AFT ages. In case of bias induced by a poor mica image for some grains, this would imply an underestimation of Ni and even younger AFT ages. The number of dated grains per sample (~18 on average reaching as high as 95 grains for sample 17) would not be adequate for the analysis of polymodal grain-age distributions, but the dataset is anyway informative because of the unimodal distribution of most samples and the observed consistency of single grain-age data (Fig. 5). In order to better visualize the grain-age distribution of polymodal samples, radial plots also report peak ages calculated with DensityPlotter (Vermeesch 2012) and Binomfit (Brandon 2002), either considering end-member scenarios for zero-track grains (Ns=0 and Ns=1) or an "intermediate" scenario corresponding to Ns=0.5 (see supplementary Table S1 for details). Calculated age peaks are generally in agreement with trends observed in radial plots, although standard ways of calculating grain-age error do not work for small track counts (e.g., Galbraith 2005).

5.2.1 Western Foothills

In sample 3 (Tsengwen River), most apatite grains are either U-poor (~30%) or U-rich with zero tracks (~60%), and only two apatite grains display fission tracks. U-rich apatite grains define a dominant population around ~1 Ma with an outlier at ~113 Ma (Figs. 4, 5). In sample 10 (Houlong River), grains with fission tracks (50% of total apatite) would yield a central age of 9±2 Ma, but U-rich zero-track grains are also present, suggesting two populations at ~1 Ma and ~14 Ma.

5.2.2 Slate Belt

In samples 2 and 5 (Laonong and upper Zhuoshui Rivers) only few grains display fission tracks. Both samples show a dominant age peak younger than 4 Ma, with a single outlier at ~15 Ma in sample 2 (Figs. 4, 5). Sample 12 (Lanyang River) is dominated by U-poor apatite grains, associated with U-rich zero-track grains pointing to an age < 3 Ma (Fig. 4). In sample 22 (Dazhu River), only two apatite grains display fission tracks that define, together with the abundant zero-track grains, a prominent AFT age peak <3 Ma, with a single outlier at ~27 Ma. The U-bearing zero-track grains of sample 9 (upper Da'an River draining the Hsueshan Range; Fig. 2) point to a single age peak around ~1 Ma (Figs. 4, 5).

5.2.3 Western rivers draining both Western Foothills and Slate Belt

Sample 1 (Kaoping River) contains only zero-track grains pointing to an age ≤6 Ma. Sample 4 (Zhuoshui River) is dominated by U-poor apatite and minor U-rich zero-track grains pointing to a prominent population ≤4 Ma, not much different from the upstream sample 5 (Figs. 4, 5). Samples 6 and 7 (Dadu and Dajia Rivers) contain a few grains with fission tracks that define, together with the abundant U-rich zero-track grains, age populations that are similar for both samples: ~0.8 Ma and ~28 Ma in the minimum-age scenario, and ~2.6 Ma and ~27 Ma in the maximum-age scenario for sample 6; ~0.6 Ma and ~41 Ma in the minimum-age scenario, and ~3 Ma and ~40 Ma in the maximum-age scenario

for sample 7 (Figs. 4, 5). Like the upstream sample 9, sample 8 (Da'an River) yielded fifteen U-rich zero-track grains pointing to a single grain-age population with maximum age not older than ~1.4 Ma. Sample 11 (Xindian River), sharing the same provenance, yielded only one U-rich zero-track grain and a rather imprecise age.

5.2.4 Tananao Complex and Coastal Range

In sample 16 (Shoufeng River draining the Tananao metamorphic belt), the only grain with spontaneous fission tracks would yield a poorly constrained Mesozoic-Cenozoic age, whereas the abundant U-rich zero-track grains point to a single late Miocene or even younger grain-age population, ≤ 1 Ma in the minimum-age scenario. In samples 18 and 19 (Lehe and Bie Rivers draining volcanic and sedimentary rocks of the Coastal Range) all apatite grains display fission tracks and yield peaks at ~16 Ma and ~13 Ma, respectively, with a single outlier at ~204 Ma in sample 19 (Figs. 4, 5). Sample S20 (Dingzilou River draining only Plio-Pleistocene Coastal Range sandstones) exclusively includes zero-track grains defining a single age peak ≤2 Ma.

5.2.5 Eastern rivers sourced in the Slate Belt, Tananao Complex, or Coastal Range

Samples 13 and 14 (Heping and Liwu Rivers sourced from the Slate Belt and mostly draining the Tailuko Belt) both indicate ages < 1 Ma (Figs. 4, 5). A similar age <1 Ma is provided by sample 14 that only includes zero-track grains. Samples 15, 17, and 21 (Hualian, Xiuguluan and Beinan trunk rivers) are also dominated by zero-track grains and yielded single-grain age populations pointing to 0 Ma in the minimum-age scenario and between 3 Ma and 5 Ma in the maximum-age scenario.

6. Discussion

6.1 Impact of zero-track grains on the AFT age signal

295 The detrital AFT analysis of modern sediments is an efficient way to supplement the
296 results of bedrock studies, allowing us to obtain, with a single sample, the average
297 thermochronological signature of the entire catchment. For a correct approach, however, it is
298 crucial to identify and consider all apatite grains, even more so where apatite is uncommon or
299 contains only a few tracks, if any. This is specifically true for U-bearing zero-track grains,
300 which in case of rapid ongoing exhumation may represent a large (or even the largest, as in
301 Taiwan) population containing fundamental information to constrain the exhumation patterns
302 inferred from AFT data.

303 In Taiwan, the few apatite grains with fission tracks in samples 3 and 22 may suggest
304 old AFT ages not reset during the Neogene orogeny, but the dominant U-rich zero-track
305 grains indicate that in both samples > 90% of the apatite grains were in fact reset and
306 exhumed across the partial annealing zone after 3 Ma (Fig. 4). Along the more extensively
307 exhumed eastern retro-side of the orogen, for example in samples 16 and 17 mainly derived
308 from the Tananao Complex, the few apatite grains with fission tracks would suggest unreset
309 old ages if zero-track grains of the overwhelming reset population were not properly
310 accounted for. In sample 7, apatite with fission tracks documents two groups of similar size:
311 unreset grains of Eocene age and reset grains of Plio-Pleistocene age. If all grains are
312 considered, then the age indications are unvaried, but the relative size of the two populations
313 is drastically modified, and reset grains become overwhelming (~80%).

314 Radial plots of samples 4 and 16, chiefly including zero-track grains but also older
315 grains with fission tracks that anyway belong to the same AFT age peak, reflect a situation
316 that could be encountered also in bedrock samples. In that case, non-random selection of
317 apatite grains for fission-track dating, e.g., preferred selection of grains with a greater number
318 of spontaneous tracks at the expense of U-rich zero-track grains, may cause an overestimation
319 of AFT ages in bedrock, which may possibly lead to infer that a rock reset after deposition

was instead unreset. As a major consequence, the analysis of bedrock samples may underestimate the size of the AFT reset zone. Our observations from modern-sand samples indicate that the AFT reset zone as inferred from previous bedrock studies (Fig. 1C) is indeed partly underestimated, possibly because information provided by zero-track grains was partly dismissed. The AFT reset zone is extended farther south and west to include a significant part of the Kaoping (1), Tsengwen (3), Houlong (10) and Dazhu (22) catchments (Fig. 6).

6.2 Impact of mineral fertility on provenance budgets

The relative size of the population that each source terrane contributes to the sediment system depends both on the spatial variability of erosion rates and on the fertility of the target mineral in each source. Because U-poor apatite grains yielding no induced track in the external detector cannot provide any useful age information, the effective apatite fertility (Fig. 3), rather than the total apatite fertility measured during mineral separation, should be considered in the calculation of apatite provenance budgets based on AFT analysis. This requires a proper combination of suitable separation procedures and Raman analysis as illustrated in Section 4. If the effective mineral fertility is quantified in each source area and duly accounted for, then the size of each population shed by each source can be converted into a provenance budget, eventually allowing quantification of short-term erosion rates in the sources once the total sediment load is known.

The annual production of U-poor and U-rich detrital apatite in a river catchment can be calculated by multiplying the corresponding apatite fertilities in each catchment by its area and average erosion rate. In Taiwan, both total (Fig. 2) and effective (Fig. 3) apatite fertilities span over three orders of magnitude (Fig. 7A), whereas average basin-wide erosion rates range between 1 and 20 mm/a (Dadson et al. 2003). Mineral fertility is thus the dominant factor controlling the amount of apatite delivered by each source. Its subtle effects, leading to

344 potential pitfalls in the calculation of provenance budgets, should be considered with
345 particular care.

346 The abundance of U-poor grains, and therefore the difference between total and
347 effective fertilities, may change significantly from catchment to catchment. For instance, total
348 fertility (represented by the total bar height in Fig. 7A) is 2.7 times higher in Hualian sand
349 (15) than in Heping sand (13), but effective fertility (i.e., the height of grey and black bar
350 segments in Fig. 7A) is less than half. Considering that erosion rates are similar in the two
351 catchments (Resentini et al. 2017) and that the Hualian catchment is 2.7 times larger (Fig.
352 7B), the amount of total apatite delivered to the Philippine Sea by the Hualian River should
353 be 7 times higher, but the amount of U-rich apatite is about the same (only 1.3 times higher)
354 and the amount of apatite with fission tracks much less and virtually null (Fig. 7C,D).

355 If we confront river systems draining opposite sides of the orogen, then we see that the
356 pro-side, where unreset grains are more common, contributes 25% of grains with fission-
357 tracks but only 10% of total U-rich zero-track grains. Apatite provenance budgets and
358 inferences on erosion patterns will be ill founded and inevitably misleading if the entire
359 apatite population is not fully considered.

360 ***6.3 Relevance of zero-track grains to understand exhumation***

361 The importance of U-rich zero-track grains to understand Taiwan erosion is
362 highlighted by a comparison of detrital AFT data provided in this study with detrital AFT
363 data recently published for the Bengal Fan (Huyghe et al. 2020). When plotted in an AFT age
364 vs [U] diagram (Fig. 8A), it emerges that apatite grains from Taiwan (in red) are dominated
365 by U-rich zero-track grains (empty dots) rather than grains with fission tracks (full dots).
366 Instead, in Bengal Fan sediments (in grey), grains with fission tracks are three times more
367 abundant than zero-track grains. About half of the U-rich zero-track grains in Taiwanese

368 samples have enough [U] to provide reliable AFT age constraints to exhumation. Several
369 zero-track grains have very low [U], ranging from 0.1 to 1 ppm. Apatite grains with very low
370 [U] are potentially present also in Bengal Fan samples but were not reported by Huyghe et al.
371 (2020), possibly because they are difficult to detect by inspection of the grain mount or
372 external detector using the optical microscope only. Although the age constraints provided by
373 these grains are rather poor, this demonstrates the effectiveness of an approach based on
374 apatite identification by Raman spectroscopy.

375 The frequency distribution of apatite grains as a function of [U] is illustrated in Fig.
376 8B. For a better comparison with Bengal Fan data, the red solid line indicates the frequency
377 distribution of apatites from Taiwan when grains with [U] < 1 ppm are not included. Taiwan
378 and Bengal Fan apatites show similar frequency distributions for [U]>1 ppm, although a
379 slightly lower modal value characterizes Taiwan samples. However, this difference does not
380 explain the overwhelming abundance of zero-track grains in Taiwan compared to the Bengal
381 Fan. The frequency distribution of apatite grains as a function of AFT age is shown in Fig.
382 8C. Two different [U] ranges (1-10 ppm and 10-100 ppm) are presented separately, because
383 apatite grains in the latter range can provide reliable AFT age constraints even if spontaneous
384 tracks are lacking. For both ranges, Taiwan data include a much greater proportion of young
385 AFT ages. This indicates that the absence of spontaneous tracks in many apatite grains form
386 Taiwan is mainly due to a short residence time below the temperature of total AFT annealing,
387 and not to low [U] as suggested by Kirstein et al. (2010). Zero-track grains thus provide first-
388 order constraints to Taiwan exhumation that must be duly considered for a correct geologic
389 interpretation.

390 **7. Ongoing southward propagation of Taiwan exhumation**

391 The tectonic framework of oblique collision between the Chinese passive continental
392 margin and the Luzon magmatic arc (Suppe 1981; Byrne et al. 2011; Simoes et al. 2012)
393 would imply southward propagation of fast exhumation across the Taiwan orogen during the
394 late Neogene. Because of very fast exhumation, bedrock ZFT and AFT data in Taiwan
395 mainly record the latest stages of the orogeny, whereas the early stages of mountain growth
396 are recorded in Plio-Pleistocene successions exposed for example in the Coastal Range
397 (Kirstein et al. 2010, 2014).

398 In the northern Coastal Range, detrital ZFT age distributions in sediments older than
399 ~2 Ma are markedly polymodal, with several moving age peaks generally older than 50 Ma
400 (Kirstein et al. 2010). Much younger ZFT age peaks are found in sediments younger than 2
401 Ma. These young peaks become progressively larger moving up section, and overwhelming
402 in modern sediments (e.g., Fellin et al. 2017). The lower part of the Plio-Pleistocene
403 succession of the northern Coastal Range would thus reflect the early-stage removal of
404 sedimentary cover rocks during the onset of arc-continent collision. The onset of fast erosion
405 can be constrained as late Miocene, whereas the removal of the rock pile with a
406 thermochronologic fingerprint acquired before the onset of arc-continent collision was likely
407 completed by 2 Ma (Malusà and Fitzgerald 2020). In the southern Coastal Range, sediments
408 from the 2-1 Ma stratigraphic interval are dominated by old ZFT age peaks (Kirstein et al.
409 2014), which indicates that the rock pile with a thermochronologic fingerprint acquired
410 before the onset of arc-continent collision was not completely removed 1 m.y. ago. However,
411 it is now completely eroded away, as attested by bedrock ZFT data (e.g., Lee at al. 2015).
412 The north-south delay in the removal of unreset sedimentary cover rocks as revealed by
413 detrital ZFT data is consistent with southward propagation of arc-continent collision (Byrne
414 et al. 2011). In the late Miocene, fast erosion rates may have affected the accretionary wedge
415 in front of the northern Coastal Range, followed 1 m.y. later by rapid erosion of the

accretionary wedge in front of the southern Coastal Range (Malusà and Fitzgerald 2020), whereas the southernmost part of Taiwan still lays outside of the ZFT reset zone (e.g., Fuller et al. 2006) (Fig. 6).

This picture can be refined using our detrital AFT data set. Unlike the concentric fission-track reset zones for zircon and apatite, shown in most previous studies to close symmetrically to the north and south (Fig. 2) and inferred by some to indicate synchronous collision from north to south (Mesalles et al. 2014; Lee et al. 2015), the AFT reset zone in Taiwan is here documented to include also the southernmost part of the island (Fig. 7). This suggests that exhumation proceeds southward, progressively exposing rocks with fully reset AFT and ZFT ages. Rapid exhumation is now affecting also the southernmost part of the island, as revealed by detrital AFT data provided that zero-track grains are properly considered. This process is not reflected yet by ZFT data, because the crustal column with ZFT ages attained before arc-continent collision is still undergoing erosional exhumation. Ongoing rapid exhumation of southernmost Taiwan is consistent with the pattern of basin-wide erosion rates inferred from gauged sediment-load data (Dadson et al. 2003). Both along the pro-side and the retro-side of the island, these values show a progressive increase from north to south, where erosion rates reach as high as 20 mm/a on the retro-side of the orogen (Fig. 6). Erosion rates are anyway higher in the backbone of the island, as also suggested by fluvial channel morphology (Chen et al. 2015) and in situ cosmogenic nuclides (Derrieux et al. 2014).

8. Application of the Taiwan approach to the Bengal Fan

The lesson learnt from detrital AFT analysis of Taiwan sediments can be applied to the interpretation of Bengal Fan AFT data recently published by Huyghe et al. (2020). Bengal Fan data reflect erosion of the central-eastern Himalaya and can be used to constrain its

exhumation history. The Himalaya includes different subparallel tectonic domains separated by north-dipping crustal-scale faults (Yin and Harrison 2000) (Fig. 9A). At either end of the orogen, the Indus and Yarlung-Brahmaputra rivers cut across crustal-scale antiforms (Nanga Parbat and Namche Barwa syntaxes). There, exposure of high-grade rocks and anatectic granites as young as the Plio-Pleistocene indicates extremely fast erosion (Zeitler et al. 2001), as reflected by very young thermochronologic ages in bedrock and modern sediments (e.g., Gemignani et al. 2018). Bengal Fan sediments collected during the International Ocean Discovery Program (IODP) Expedition 354 (France-Lanord et al. 2016) have been the target of a multimethod detrital thermochronology study also including ZFT dating, which has revealed polymodal ZFT age distributions attesting to a mixed provenance, with the youngest peaks likely reflecting fast erosion of the Namche Barwa syntaxis (Najman et al. 2019). However, the AFT signal of fast syntaxial exhumation was not detected either in samples collected during the IODP Expedition 354 (Huyghe et al. 2020) or in distal Bengal Fan samples collected during the Ocean Drilling Program Leg 116 (Corrigan and Crowley 1990). As suggested by Malusà and Fitzgerald (2020), this may be ascribed either to a fertility bias or to the underestimation of zero-track grains during analysis and subsequent data interpretation. Figure 9B shows, on the left, the mid-Bengal Fan lag-time diagram based on AFT central ages as proposed by Huyghe et al. (2020). These authors have excluded part of the central ages from lag-time interpretation (in grey in Fig. 9B) because they are younger than the sample's depositional age, despite sedimentary burial (<900 m for most of the samples) is insufficient to induce any AFT age rejuvenation by post-depositional annealing. Alternatively, this may suggest depositional-age overestimation based on biostratigraphy. However, the most remarkable feature of this lag-time diagram is that most of the other central ages, indicated in blue, are older than the youngest ZFT age peak (indicated by the small red dots) reflecting fast exhumation of the Namche Barwa syntaxis (Najman et al.

2019). This is geologically paradoxical, because the AFT system has lower closure temperature than the ZFT system. Therefore, AFT ages should be younger than ZFT ages for grains derived from the same source. In the Bengal Fan case, a lag-time analysis based on central ages is thus geologically meaningless, because information from a rapidly exhuming source (the Namche Barwa syntaxis) and from other regions eroded at slower rates is inevitably mixed. Moreover, the AFT grain-age distributions in many Bengal Fan samples are markedly bimodal (Fig. 9C), which indicates that geologic interpretation can be significantly improved by deconvolution of grain-age distributions in individual peaks. AFT age peaks calculated with DensityPlotter (Vermeesch 2012) and Binomfit (Brandon 2002) following the same procedure described for the Taiwan samples are shown in Fig. 9B (see supplementary Table S2 for details). The smaller circles in the diagrams to the right indicate AFT age peaks calculated for a minimum-age scenario (i.e., Ns=0 for zero-track grains), whereas the bigger circles indicate the AFT age peaks calculated for a maximum-age scenario (i.e., Ns=1 for zero-track grains). For both scenarios, the youngest AFT age peaks are consistent (red outlines) with the youngest ZFT age peaks in the same stratigraphic level, which means that they likely reflect fast exhumation of the Namche Barwa syntaxis. If zero-track grains are properly considered, then the size of these peaks is dominant in the AFT distribution (see color scale on the top right), pointing to a major role of the Namche Barwa syntaxis as a source of apatite grains shed to the Bengal Fan.

9. Conclusions

The analysis of Taiwan modern sands demonstrates the importance of effective apatite fertility measurements and of accurate detection of zero-track apatite grains for a correct geologic interpretation of detrital AFT data. The effectiveness of Raman spectroscopy for apatite-grain identification is also highlighted. U-rich zero-track grains are dominant in the Taiwan data set, and generally contain enough U to provide reliable constraints to

exhumation timing. The absence of spontaneous tracks in most of these grains is mainly due to a short residence time below the temperature of total AFT annealing rather than to low [U], which confirms that zero-track grains must be duly accounted for to understand tectonic-related exhumation in Taiwan. Our observations from sediment samples indicate that the Taiwan AFT reset zone determined from the analysis of bedrock samples was partly underestimated, probably because information provided by zero-track grains was overlooked. If combined with ZFT data from the Plio-Pleistocene succession of the Coastal Range, then the AFT reset zone here documented to include the southernmost part of the island provides additional support to previous studies suggesting southward-progressing exhumation during oblique arc-continent collision. The lesson learnt from Taiwan helps to better understand Himalayan exhumation, pointing to a major role of the Namche Barwa syntaxis as a major source of apatite grains shed to the Bengal Fan.

Acknowledgments The manuscript benefited from comments to a previous version by Tim Byrne and three anonymous reviewers. E.G. heartily thanks Seb Castelltort for introducing him to the geology of Taiwan, Andrew Tien-Shun Lin for hospitality at Chongli, and Pei-Hua Hsu and Ming-Wei Liao for fundamental assistance in the field. Funding provided by Project MIUR-PRIN 2015EC9PJ5 “The subduction and exhumation of the continental lithosphere: their effects on the structure and evolution of the orogens”.

References

Baldwin, S.L., Fitzgerald, P.G., Malusà, M.G., 2019. Crustal Exhumation of Plutonic and Metamorphic Rocks: Constraints from Fission-Track Thermochronology. In: Malusà, M.G., Fitzgerald, P.G. (Eds.), Fission-Track Thermochronology and its Application to Geology, Springer Textbooks in Earth Sciences, Geography and Environment, ch.13, pp. 235-257.

513 Bardsley, W. E., 1983. Confidence limits for fission-track dating. Journal of the International
514 Association for Mathematical Geology, 15(6), 649-658.

515 Beyssac, O., Simoes, M., Avouac, J.P., Farley, K.A., Chen, Y.G., Chan, Y.C., Goffé, B.,
516 2007. Late Cenozoic metamorphic evolution and exhumation of Taiwan, Tectonics, 26,
517 TC6001.

518 Beyssac, O., Negro, F., Simoes, M., Chan, Y.C., Chen, Y.G., 2008. High-pressure
519 metamorphism in Taiwan: from oceanic subduction to arc-continent collision? Terra Nova,
520 20(2), 118-125.

521 Brandon, M. T., 2002. Decomposition of mixed grain age distributions using Binomfit. On
522 track, 24(8), 13-18.

523 Byrne, T., Chan, Y.C., Rau, R.J., Lu, C.Y., Lee, Y.H., Wang, Y.J., 2011. The arc–continent
524 collision in Taiwan. In: Brown, D., Ryan, P.D. (Eds.), Arc-Continent Collision Springer,
525 Berlin-Heidelberg, pp. 213-245.

526 Central Geological Survey, Ministry of Economic Affairs, 2000. Geological map of Taiwan
527 1:500000, Taipei.

528 Chen, Y.-W., Shyu, J. B. H., Chang C.-P., 2015. Neotectonic characteristics along the eastern
529 flank of the Central Range in the active Taiwan orogen inferred from fluvial channel
530 morphology. Tectonics, 34, 2249-2270, doi:10.1002/2014TC003795

531 Corrigan, J. D., Crowley, K. D., 1990. Fission-track analysis of detrital apatites from sites
532 717 and 718, Leg 116, Central Indian Ocean. In Proc. Ocean Drill. Program Sci. Results,
533 vVol. 116, pp. 75-92.

534 Dadson, S.J., Hovius, N., Chen, H., Dade, W.B., Hsieh, M.L., Willett, S.D., Hu, J.D., Horng,
535 M.J., Chen, M.C., Stark, C.P., Lague, D., Lin, J.C., 2003. Links between erosion, runoff
536 variability and seismicity in the Taiwan orogen. Nature, 426, 648-651.

537 Derrieux, F., Siame, L. L., Bourlès, D. L., Chen, R. F., Braucher, R., Léanni, L., ... Byrne, T.
538 B., 2014. How fast is the denudation of the Taiwan mountain belt? Perspectives from in situ
539 cosmogenic 10Be. Journal of Asian Earth Sciences, 88, 230-245.

540 Dorsey, R.J., 1988. Provenance evolution and unroofing history of a modern arc-continent
541 collision; evidence from petrography of Plio-Pleistocene sandstones, eastern Taiwan. Journal
542 of Sedimentary Research, 58(2), 208-218.

543 Fellin, M.G., Chen, C.Y., Willett, S.D., Christls, M., Chen, Y.G., 2017. Erosion rates across
544 space and timescales from a multi-proxy study of rivers of eastern Taiwan. Global and
545 Planetary Change, 157, 174-193.

546 France-Lanord, C., Spiess, V., Klaus, A., Schwenk, T., 2016. the Expedition 354 Scientists.
547 Proceedings of the International Ocean Discovery Program. Bengal Fan, 354.

548 Fuller, C.W., Willet, S.D., Fisher, D., Lu, C.Y., 2006. A thermomechanical wedge model of
549 Taiwan constrained by fission-track thermochronometry. Tectonophysics, 274, 97–115.

550 Galbraith, R.F., 2005. Statistics for fission track analysis. Chapman and Hall/CRC, Boca
551 Raton FL, 240 p.

552 Garzanti, E., 2019. The Himalayan Foreland Basin from collision onset to the present: a
553 sedimentary–petrology perspective. Geological Society, London, Special Publications, 483,
554 SP483-17.

555 Gemignani, L., van der Beek, P. A., Braun, J., Najman, Y., Bernet, M., Garzanti, E.,
556 Wijbrans, J. R., 2018. Downstream evolution of the thermochronologic age signal in the

557 Brahmaputra catchment (eastern Himalaya): Implications for the detrital record of erosion.
558 Earth and Planetary Science Letters, 499, 48-61.

559 Harlov, D. E., 2015. Apatite: a fingerprint for metasomatic processes. Elements, 11(3), 171-
560 176.

561 Hsu, W. H., Byrne, T.B., Ouimet, W., Lee, Y.H., Chen, Y.G., Soest, M.V., Hodges, K., 2016.
562 Pleistocene onset of rapid, punctuated exhumation in the eastern Central Range of the Taiwan
563 orogenic belt. Geology, 44, 719-722.

564 Huang, C.Y., Yuan, P.B., Tsao, S.J., 2006. Temporal and spatial records of active arc-
565 continent collision in Taiwan: a synthesis. Geological Society of America Bulletin, 118, 274–
566 288.

567 Huyghe, P., Bernet, M., Galy, A., Naylor, M., Cruz, J., Gyawali, B.R., Mugnier, J.L., 2020.
568 Rapid exhumation since at least 13 Ma in the Himalaya recorded by detrital apatite fission-
569 track dating of Bengal fan (IODP Expedition 354) and modern Himalayan river sediments.
570 Earth and Planetary Science Letters, 534, 116078.

571 Kirstein, L.A., Fellin, M.G., Willett, S.D., Carter, A., Chen, Y.G., Garver, J.I., Lee, D.C.,
572 2010. Pliocene onset of rapid exhumation in Taiwan during arc-continent collision: new
573 insights from detrital thermochronometry. Basin Research, 22, 270–285.

574 Kirstein, L.A., Carter, A., Chen, Y.G., 2014. Impacts of arc collision on small orogens: new
575 insights from the Coastal Range detrital record, Taiwan. Journal of the Geological Society,
576 171(1), 5-8.

577 Kohn, B., Chung, L., Gleadow, A., 2019. Fission-track analysis: field collection, sample
578 preparation and data acquisition. In Fission-Track Thermochronology and its Application to
579 Geology (pp. 25-48). Springer, Cham.

580 Lee, Y.H., Chen, C.C., Liu, T.K., Ho, H.C., Lu, H.Y., Lo, W., 2006. Mountain building
581 mechanisms in the Southern Central Range of the Taiwan Orogenic Belt — From
582 accretionary wedge deformation to arc– continental collision. Earth and Planetary Science
583 Letters, 252, 413– 422.

584 Lee, Y.H., Byrne, T., Wang, W.H., Lo, W., Rau, R.J., Lu, H.Y., 2015. Simultaneous
585 mountain building in the Taiwan orogenic belt. Geology, 43, 451-454.

586 Liu, T.K., Hsieh, S., Chen, Y.G., Chen, W.S. 2001. Thermo-kinematic evolution of the
587 Taiwan oblique-collision mountain belt as revealed by zircon fission-track dating. Earth and
588 Planetary Science Letters, 186, 45–56.

589 Malusà, M.G., Resentini, A., Garzanti E., 2016. Hydraulic sorting and mineral fertility bias in
590 detrital geochronology. Gondwana Research, 31, 1–19.

591 Malusà, M.G., Wang, J., Garzanti, E., Liu, Z.C., Villa, I.M., Wittmann, H., 2017. Trace-
592 element and Nd-isotope systematics in detrital apatite of the Po river catchment: Implications
593 for provenance discrimination and the lag-time approach to detrital thermochronology.
594 Lithos, 290-291, 48-59.

595 Malusà, M.G., Fitzgerald, P.G. (Eds.), 2019. Fission-track thermochronology and its
596 application to geology. Springer Textbooks in Earth Sciences, Geography and Environment,
597 393 pp.

598 Malusà, M.G., Fitzgerald, P.G., 2020. The geologic interpretation of the detrital
599 thermochronology record within a stratigraphic framework, with examples from the
600 European Alps, Taiwan and the Himalayas. Earth-Science Reviews, 103074, doi:
601 10.1016/j.earscirev.2019.103074

602 Malusà, M.G., Garzanti E., 2019. The sedimentology of detrital thermochronology. In:
603 Malusà, M.G., Fitzgerald, P.G. (Eds.), Fission-Track Thermochronology and its Application
604 to Geology, Springer Textbooks in Earth Sciences, Geography and Environment, ch.7,
605 pp.123-143.

606 Mesalles, L., Mouthereau, F., Bernet, M., Chang, C.P., Lin, A., Fillon, C., Sengelen, X.,
607 2014. From submarine continental accretion to arc-continent orogenic evolution: The thermal
608 record in southern Taiwan. Geology, 42, 907-910.

609 Mouthereau, F., Deffontaines, B., Lacombe, O., Angelier, J., 2002. Variations along the
610 strike of the Taiwan thrust belt: Basement control on structural style, wedge geometry, and
611 kinematics. In: Byrne, T.B., Liu, C.S. (Eds.), Geology and Geophysics of an Arc-Continent
612 collision, Taiwan, Republic of China: Boulder, Colorado, Geological Society of America
613 Special Paper 358, pp.35–58.

614 Najman, Y., Mark, C., Barfod, D. N., Carter, A., Parrish, R., Chew, D., Gemignani, L., 2019.
615 Spatial and temporal trends in exhumation of the Eastern Himalaya and syntaxis as
616 determined from a multitechnique detrital thermochronological study of the Bengal Fan.
617 Geological Society of America Bulletin, 131(9-10), 1607-1622.

618 O'Sullivan, G., Chew, D., Kenny, G., Henrichs, I., Mulligan, D., 2020. The trace element
619 composition of apatite and its application to detrital provenance studies. Earth-Science
620 Reviews, 103044.

621 Resentini, A., Malusà, M. G., Garzanti, E., 2013. MinSORTING: An Excel® worksheet for
622 modelling mineral grain-size distribution in sediments, with application to detrital
623 geochronology and provenance studies. Computers & geosciences, 59, 90-97.

624 Resentini, A., Goren, L., Castelltort, S., Garzanti, E., 2017. Partitioning sediment flux by
625 provenance and tracing erosion patterns in Taiwan. Journal of Geophysical Research: Earth
626 Surface, 122, 1430-1454.

627 Reiners, P. W., Ehlers, T. A. (Eds.), 2018. Low-temperature thermochronology: Techniques,
628 interpretations, and applications. Reviews in Mineralogy and Geochemistry, 58,
629 Mineralogical Society of America.

630 Simoes, M., Beyssac, O., Chen, Y.G., 2012. Late Cenozoic metamorphism and mountain
631 building in Taiwan: A review. Journal of Asian Earth Sciences, 46, 92-119.

632 Suppe, J., 1981. Mechanics of mountain-building and metamorphism in Taiwan. Geological
633 Society of China Memoir, 4, 67-89.

634 Tsao, S.J., 1996. The geological significance of illite crystallinity, zircon fission-track ages
635 and K-Ar ages of metasedimentary rocks of the Central Range. Ph.D. thesis, National Taiwan
636 University, Taipei, pp. 272.

637 Vermeesch, P., 2012. On the visualisation of detrital age distributions. Chemical Geology
638 312-313, 190–194.

639 Wagner G.A., van den Haute P., 1992. Fission-track dating. Kluwer Academic Publishers,
640 Dordrecht, Solid Earth Sciences Library, v.6, 285 p.

641 Willett, S.D., Fisher, D. M. Fuller, C.W. En-Chao, Y. Chia-Yu, L., 2003. Erosion rates and
642 orogenic-wedge kinematics in Taiwan inferred from fission-track thermochronometry.
643 Geology, 31, 945–948.

644 Yin, A., Harrison, T. M., 2000. Geologic evolution of the Himalayan-Tibetan orogen. Annual
645 review of earth and planetary sciences, 28(1), 211-280.

646 Yui, T.F., Maki, K., Lan, C.Y., Hirata, T., Chu, H.T., Kon, Y., Yokoyama, T.D., Jahn, B.M.,
647 Ernst, W.G., 2012. Detrital zircons from the Tananao metamorphic complex of Taiwan:
648 Implications for sediment provenance and Mesozoic tectonics. Tectonophysics, 541-543, 31-
649 42.

650 Zeitler, P.K., Meltzer, A.S., Koons, P.O., Craw, D., Hallet, B., Chamberlain, C.P., Kidd,
651 W.S., Park, S.K., Seeber, L., Bishop, M., Shroder, J., 2001. Erosion, Himalayan
652 geodynamics, and the geomorphology of metamorphism. GSA Today, 11(1), 4-9.

653

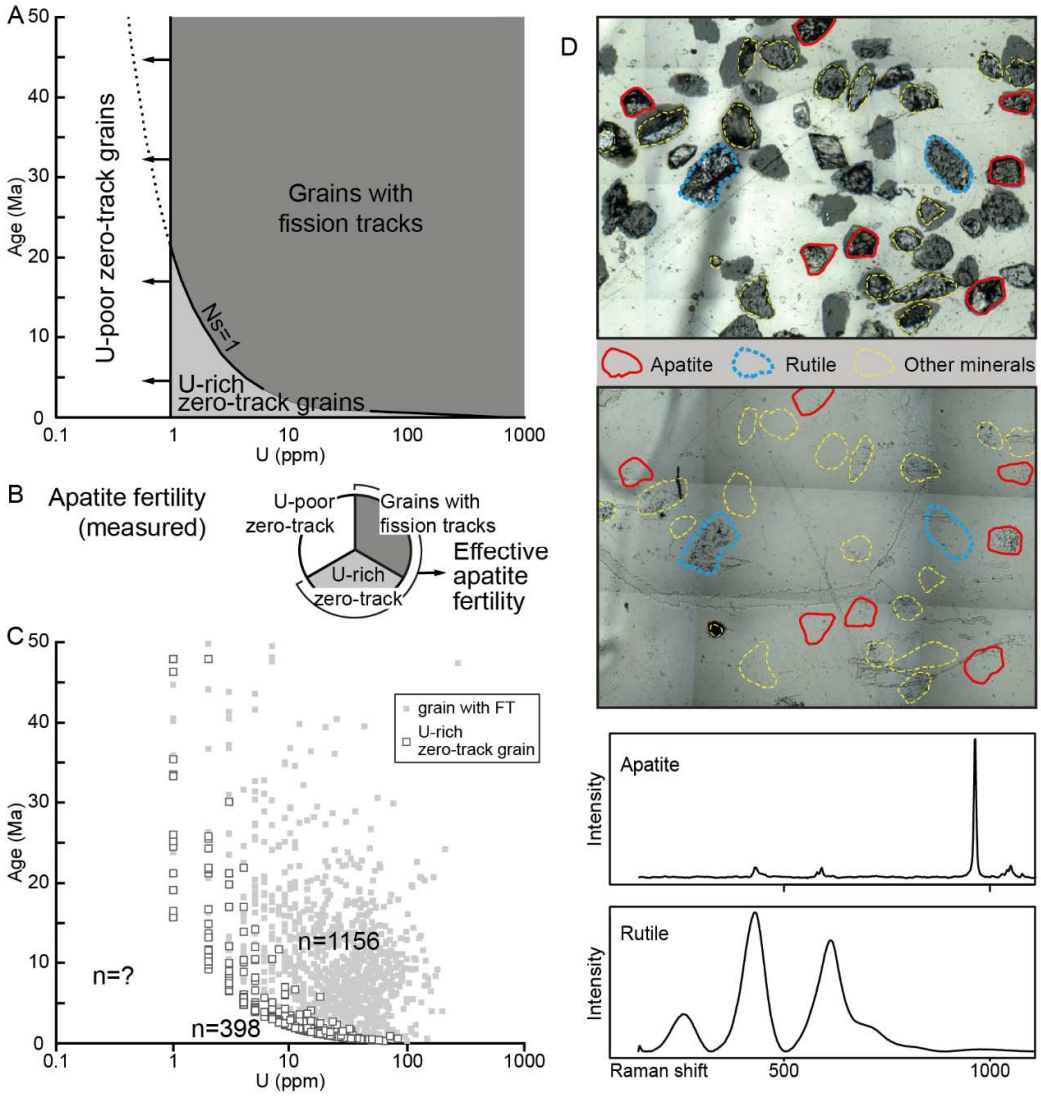

Figure 1. Fission-track characteristics of apatite grains. A) AFT age vs [U] diagram showing the fields of different types of AFT grains (field boundary for grains with fission tracks calculated for: ρ_D=9.1188×10^5, area=0.01 mm^2, ζ=295.8). U-rich zero-track grains encompass an age range between 0 Ma and a maximum age corresponding to Ns=1, which becomes narrower for increasing [U]; the field of U-poor zero-track grains is smaller for stronger irradiations. **B)** Relationships between total and effective apatite fertilities and different types of AFT grains. The total apatite fertility measured during mineral separation includes undatable U-poor zero-track grains that are not relevant for detrital

thermochronology studies. **C)** AFT age vs [U] diagram for apatite grains of the Bengal Fan (based on data from Huyghe et al. 2020); U-rich zero-track grains are plotted as Ns=0.5 (the amount of U-poor zero-track grains was not determined). **D)** Raman spectroscopy identification of apatite grains and other minerals (e.g., rutile) that induce tracks in the external detector.

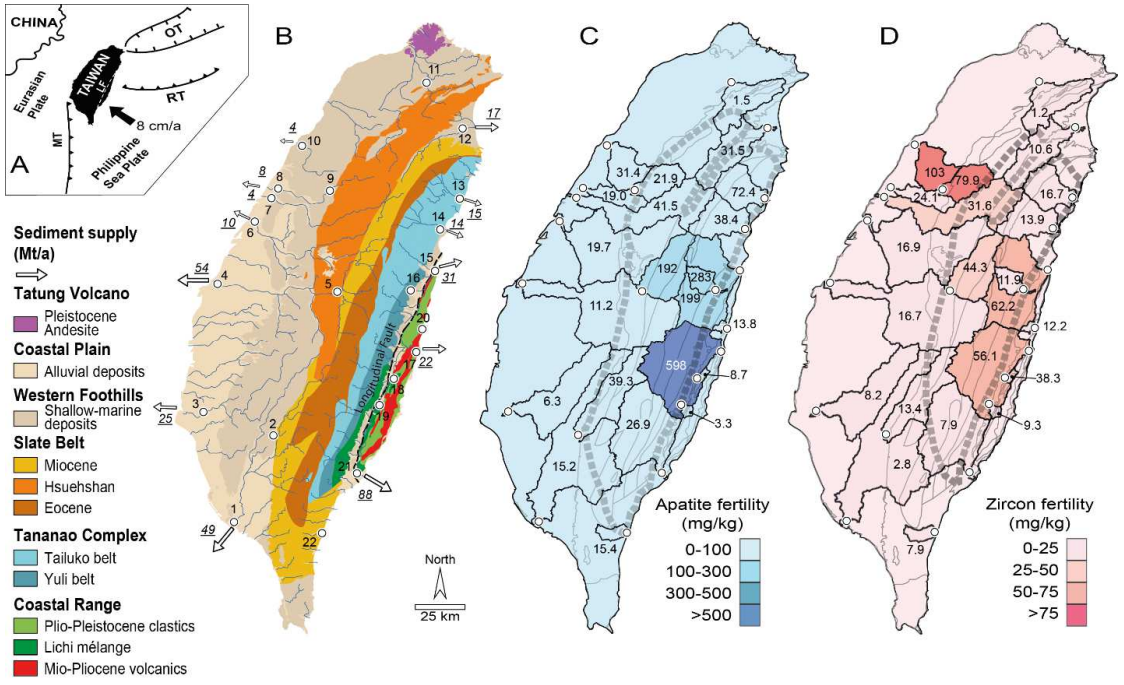

Figure 2. The Taiwan orogen. A) Geodynamic setting: LF Longitudinal Fault; MT Manila Trench; OT Okinawa Trench; RT Ryukyu Trench; **B)** Tectonic domains (Central Geological Survey 2000) and sampling sites of river sands (1 Kaoping, 2 Laonong, 3 Tsengwen, 4+5 Zhuoshui, 6 Dadu, 7 Dajia, 8+9 Da'an, 10 Houlong, 11 Xindian, 12 Lanyang, 13 Heping, 14 Liwu, 15 Hualian, 16 Shoufeng, 17 Xiuguluan, 18 Lehe, 19 Bie, 20 Dingzilou, 21 Beinan, 22 Dazhu). Sediment load data (in Mt/a, white arrows) after Dadson et al. (2003); **C-D)** Total apatite and zircon fertility maps based on the concentration of detrital apatite and zircon in analysed modern-sand samples. The grey dashed lines indicate the fission-track reset zones for apatite and zircon (Fuller et al. 2006).

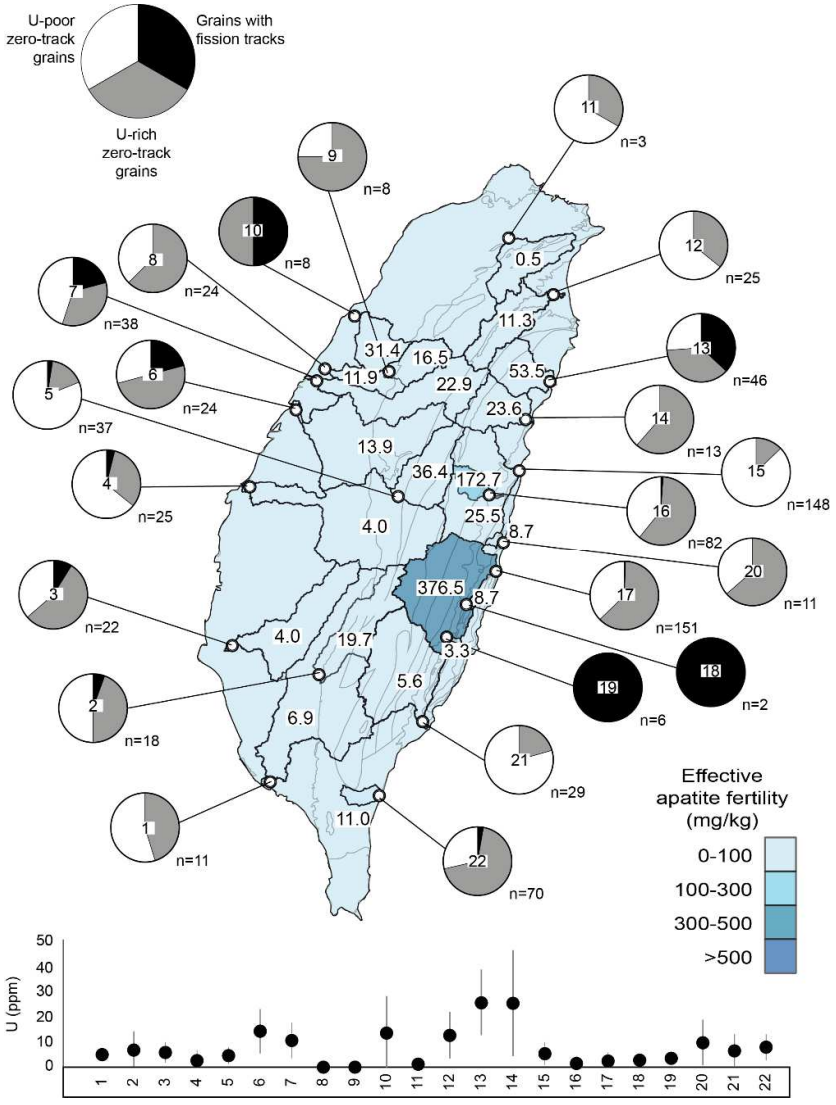

Figure 3. Distribution of detrital apatite types. Main panel: effective apatite fertility map and pie charts indicating the relative proportions of different apatite types in each sample (different proportions reflect different lithology and metamorphic grade of the source rocks); n = number of identified apatite grains per sample (the sample number is indicated in the centre of each chart). Lower panel: average [U] and standard deviation (error bar) in apatite grains from each sample.

691

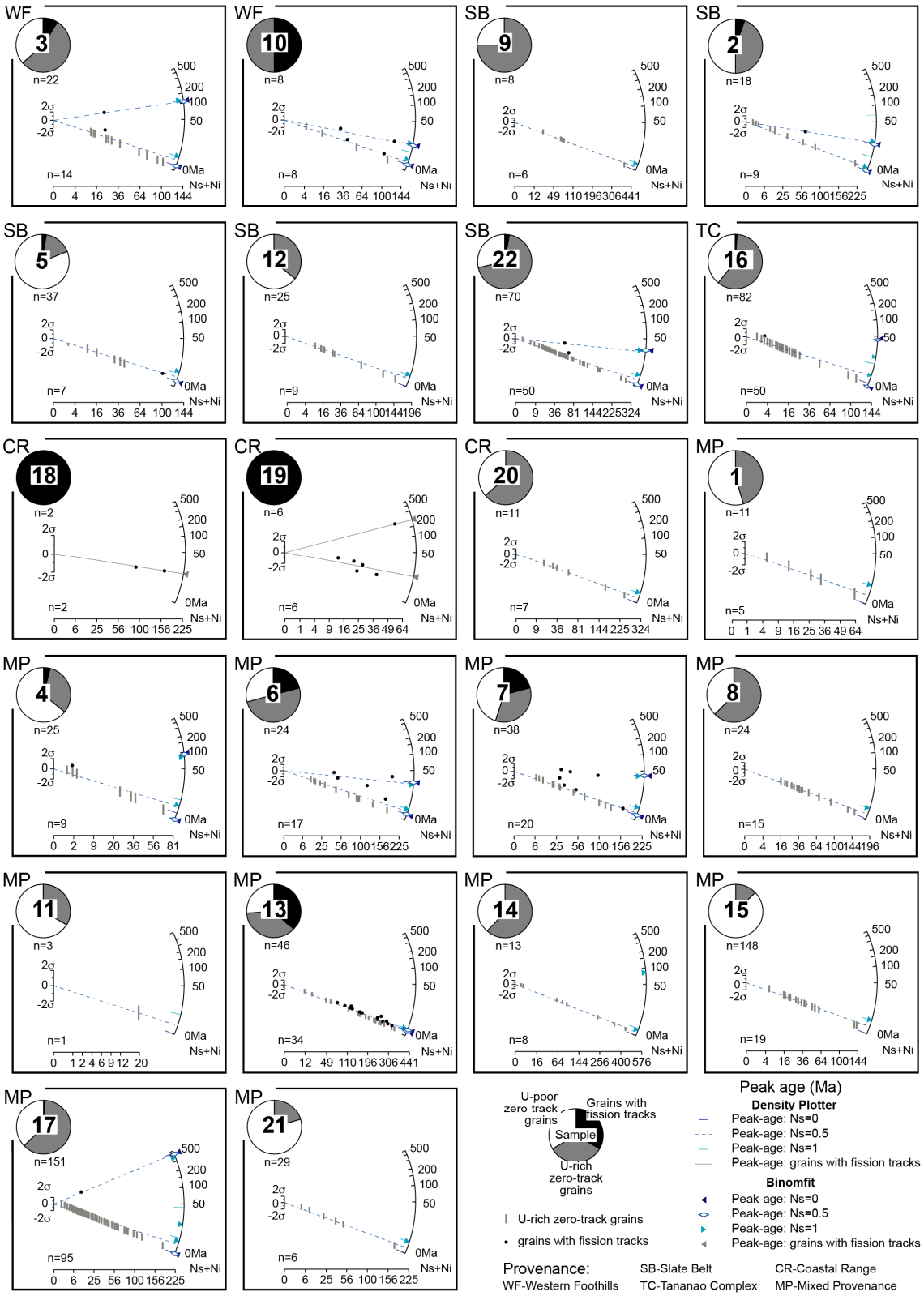
WF
3
n=22
n=14
0 4 16 36 64 100 144
WF
10
n=8
n=8
0 4 16 36 64 100144
SB
9
n=8
n=6
0 12 49 110196306441
SB
2
n=18
n=9
0 6 25 56 100156225
SB
5
n=37
n=7
0 4 16 36 64 100 144
SB
12
n=25
n=9
0 4 16 36 64 100144196
SB
22
n=70
n=50
0 9 36 81 144225324
TC
16
n=82
n=50
0 4 16 36 64 100 144
CR
18
n=2
n=2
0 6 25 56 100 156 225
CR
19
n=6
n=6
0 1 4 9 16 25 36 49 64
CR
20
n=11
n=7
0 9 36 81 144 225 324
MP
1
n=11
n=5
0 1 4 9 16 25 36 49 64
MP
4
n=25
n=9
0 2 9 20 36 56 81
MP
6
n=24
n=17
0 6 25 56 100156225
MP
7
n=38
n=20
0 6 25 56 100 156 225
MP
8
n=24
n=15
0 4 16 36 64 100144196
MP
11
n=3
n=1
0 1 2 4 6 9 12 20
MP
13
n=46
n=34
0 12 49 110 196 306 441
MP
14
n=13
n=8
0 16 64 144 256 400 576
MP
15
n=148
n=19
0 4 16 36 64 100144
MP
17
n=151
n=95
0 6 25 56 100 156 225
MP
21
n=29
n=6
0 6 25 56 100 156 225
500
200
100
50
0Ma
Ns+Ni
2σ
0
-2σ
U-poor zero track grains
Grains with fission tracks
Sample
U-rich zero-track grains
U-rich zero-track grains
grains with fission tracks
Peak age (Ma)
Density Plotter
Peak-age: Ns=0
Peak-age: Ns=0.5
Peak-age: Ns=1
Peak-age: grains with fission tracks
Binomfit
Peak-age: Ns=0
Peak-age: Ns=0.5
Peak-age: Ns=1
Peak-age: grains with fission tracks
Provenance:
WF-Western Foothills
SB-Slate Belt
TC-Tananao Complex
CR-Coastal Range
MP-Mixed Provenance

692

693 **Figure 4. The Taiwan AFT data set – radial plots.** Grains with fission tracks are indicated
694 by full dots. U-rich zero-track grains are indicated by vertical bars encompassing the age
695 range comprised between 0 Ma (minimum-age scenario) and the age corresponding to a
696 single spontaneous track for the measured [U] (maximum-age scenario); n = number of dated
697 grains per sample. Plots also report peak ages calculated with DensityPlotter (Vermeesch
698 2012) and Binomfit (Brandon 2002), either considering end-member scenarios for zero-track
699 grains (Ns=0 and Ns=1) or an "intermediate" scenario corresponding to Ns=0.5 (see keys to
700 the bottom-right). The pie charts on the top left of each diagram indicate the proportion of
701 different apatite types (n = total number of identified apatite grains). Samples are arranged
702 according to provenance (WS, Western Foothills; SB, Slate Belt; TC, Tananao Complex; CR,
703 Coastal Range; MP, mixed provenance).

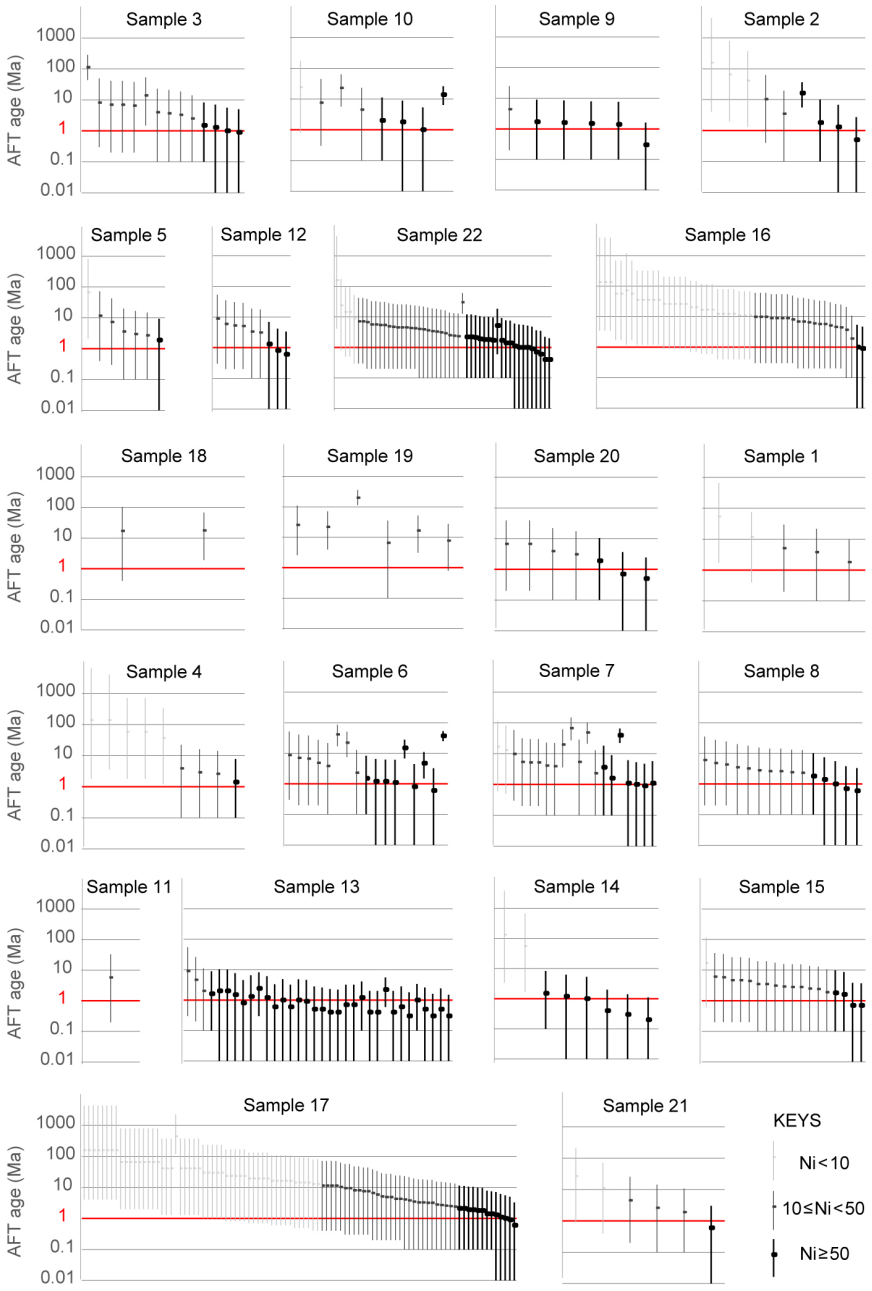

704

705 **Figure 5. Confidence intervals for single-grain ages.** Dots indicate single-grain ages (Ma)
706 for the Taiwan data set. Error bars indicate associated 95% confidence intervals calculated
707 with Binomfit (Brandon 2002). Samples are shown in the same order as in Fig. 4. In each
708 diagram, grains are arranged from lower to higher Ni, using different colors for grains with
709 Ni < 10 (light grey), grains with 10 ≤ Ni < 50 (dark grey), and grains with Ni ≥ 50 (black)
710 associated to highest precision.

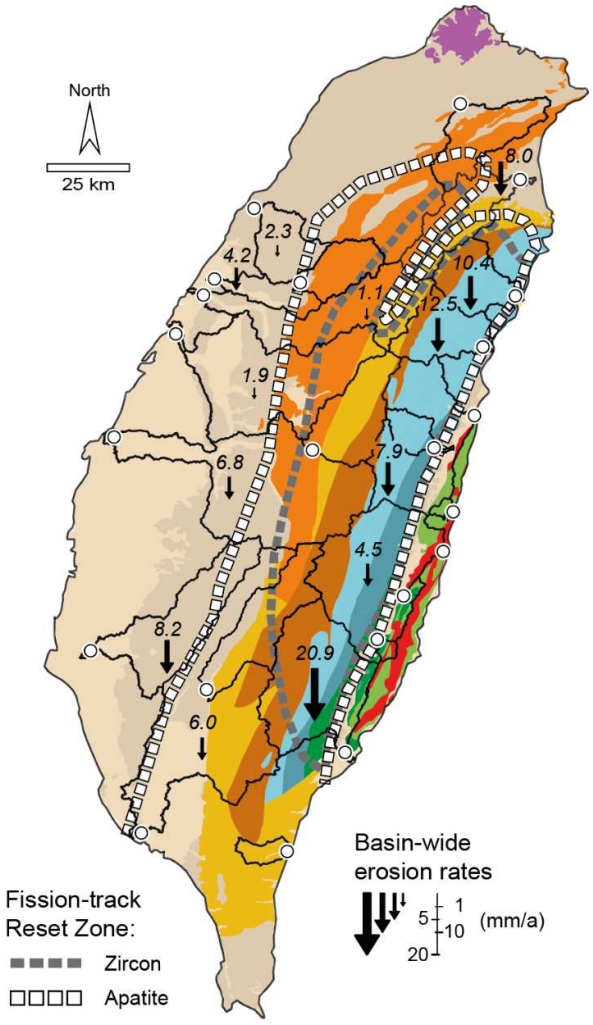

711

712 **Figure 6. Revised AFT reset zone for Taiwan.** Based on fission-track data on modern sands
713 (Fig. 4), the AFT reset zone is extended farther south and west to include a significant part of
714 the Kaoping, Tsengwen, Houlong and Dazhu catchments (ZFT reset zone after Fuller et al.
715 2006). Exposure of reset AFT ages in the southernmost island supports the hypothesis of
716 southward propagation of erosional exhumation, consistent with basin-wide erosion rates
717 (after Dadson et al. 2003) that increase southward along both the pro-side and retro-side of
718 the orogen.

719

720

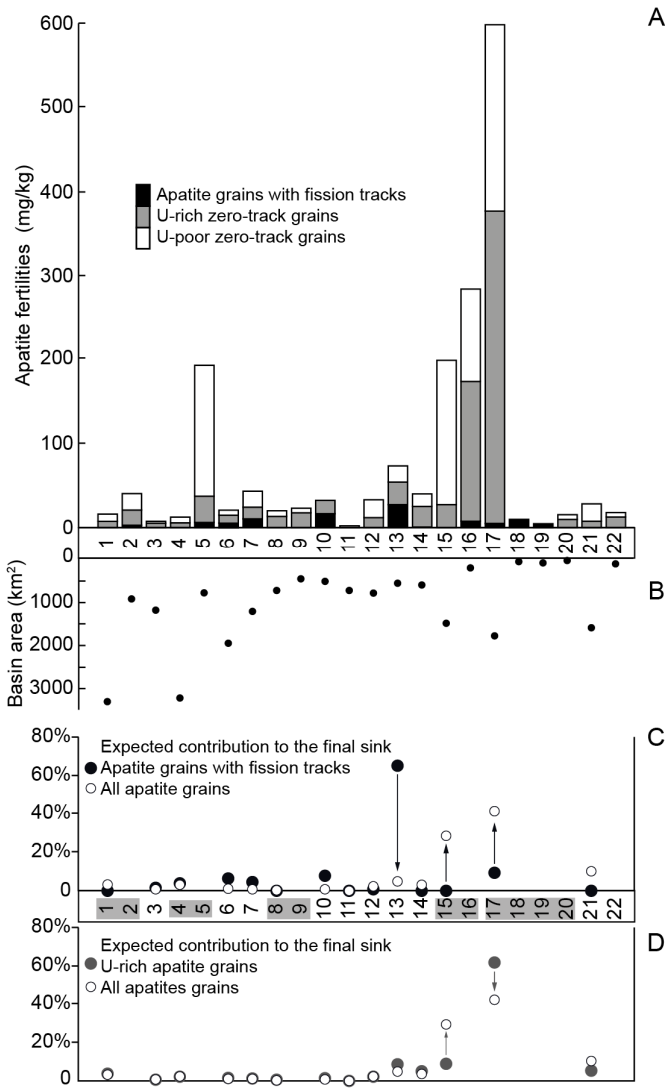

721

722 **Figure 7. Influence of total versus effective apatite fertility on provenance budgets based**
723 **on AFT data. A)** Estimated total apatite fertility in each catchment as the sum of U-poor
724 (white) and U-rich apatite grains (grey = zero-track; black = with tracks). Note that total
725 fertility varies over three orders of magnitude, and that zero-track grains are much more
726 abundant than grains with fission tracks. **B)** Catchment areas. **C, D)** Apatite contributions
727 from the studied catchments based on drainage areas, erosion rates (Dadson et al. 2003) and
728 apatite fertilities, either considering apatite grains with fission tracks *versus* all apatite grains
729 (C) or U-rich apatites *versus* all apatite grains (D). Dismissing U-rich zero-track grains leads

730 to erratically biased provenance estimates (e.g., relative apatite supply from catchment 13 is
731 strongly overestimated in C but almost correctly assessed in D, whereas supply from
732 catchment 17 is largely underestimated in C and overestimated in D).
733

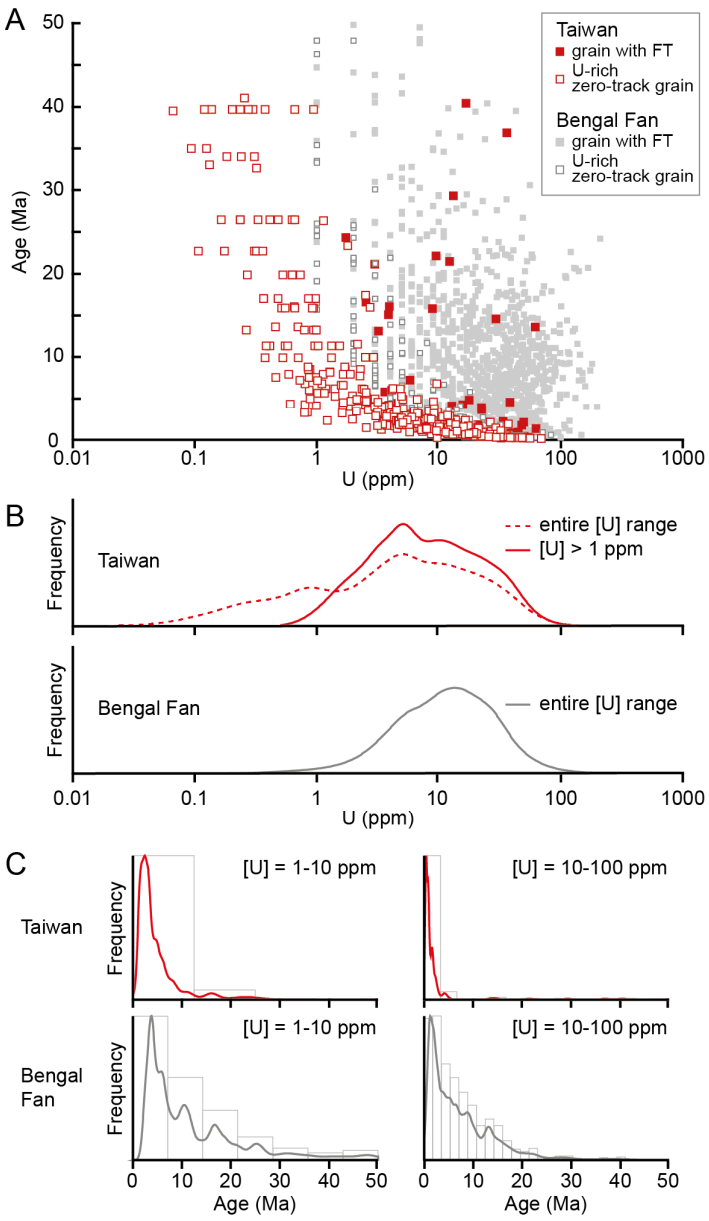

Figure 8. Comparison between Taiwan and Bengal Fan data sets. A) AFT age vs [U] diagram showing grains with fission tracks (full dots) and U-rich zero-track grains (empty dots, plotted as Ns=0.5) in data sets from Taiwan (in red, this study) and the Bengal Fan (in grey, after Huyghe et al. 2020). Unlike the Bengal Fan data set, which shows a majority of grains with fission tracks, U-rich zero-track grains are overwhelming in Taiwan and generally have enough [U] to provide reliable age constraints. The many grains with [U] < 1 ppm

742 reported from Taiwanese samples (but not from the Bengal Fan) demonstrate the
743 effectiveness of Raman spectroscopy for apatite identification. **B)** Frequency distributions of
744 detrital apatite as a function of [U]. If grains with [U] < 1 ppm are excluded (as possibly
745 present but undetected in Bengal Fan samples), then Taiwan and Bengal Fan apatites would
746 show similar frequency distributions with respect to [U], but a slightly lower modal value for
747 Taiwanese samples. **C)** Frequency distributions of detrital apatite grains as a function of AFT
748 age for different [U] ranges (1-10 ppm and 10-100 ppm). For both [U] ranges, Taiwan apatite
749 grains yield a much greater proportion of young AFT ages. This attests that lack of
750 spontaneous tracks in apatite grains form Taiwan is mainly due to a short residence time
751 below the temperature of total annealing rather than to low [U].
752

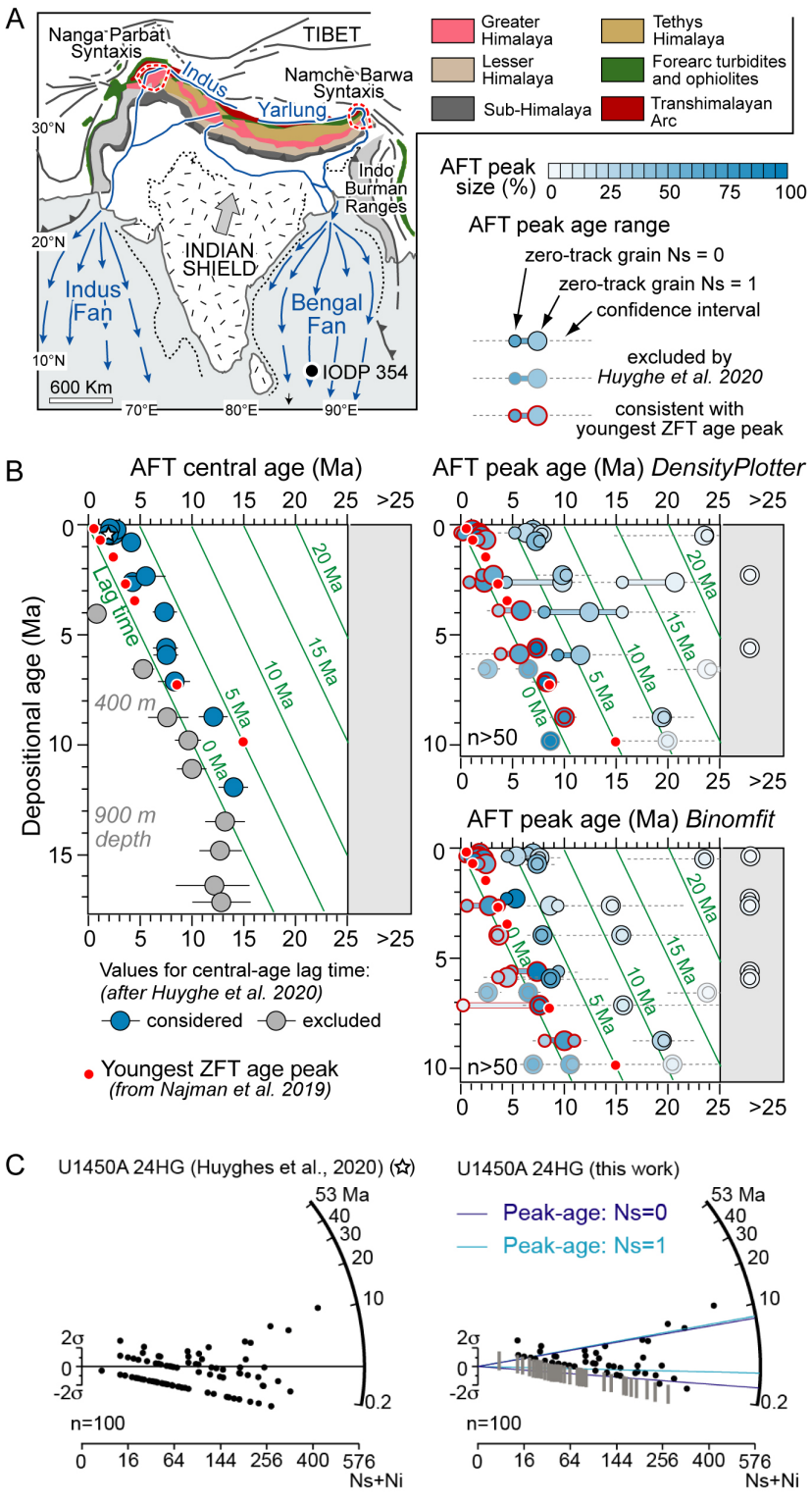

Figure 9. Reinterpretation of the Bengal Fan AFT data set. A) Tectonic sketch map of the Himalayan region and location of IODP 354 site. **B)** Lag-time diagrams for the mid-Bengal

Fan reporting AFT central ages (on the left, after Huyghe et al. 2020) and AFT peak ages (on the right, this study) calculated with DensityPlotter (Vermeesch 2012) and Binomfit (Brandon 2002). On the left, the central ages in grey were excluded from lag-time calculation by Huyghe et al. (2020) because younger than the depositional age (i.e., they would yield negative lag time despite post-depositional burial is insufficient for AFT annealing). The other central ages (in blue) are mostly older than the ZFT age of the youngest peaks reported by Najman et al. (2019) (red dots), which is geologically paradoxical. On the right, age peaks including zero-track grains are calculated for both a minimum-age scenario (Ns=0, smaller circle) and a maximum-age scenario (Ns=1, bigger circle); red outlines mark the AFT age peaks consistent with the youngest ZFT age peaks in the same stratigraphic level; color intensities indicate the size of each peak. **C)** Radial plot of single grain ages for the markedly bimodal sample U1450A 24HG (white star in the lag-time plot in B) as reported by Huyghe et al. (2020) (on the left) and as further elaborated in this study (on the right) by including the entire age range associated to U-rich zero-track grains and the age peaks calculated with DensityPlotter (dark blue = minimum-age scenario; light blue = maximum-age scenario).

773

774 **Table 1.** Detrital AFT data and central age of Taiwan samples

Sample	Analyzed grains	Ns	Ni	Rho-s	Rho-i	Central age (Ma)
S1	5	0	102	0.0000	2.3832	-
S2	9	6	474	0.0544	4.3013	2.5 ± 2.3
S3	14	12	539	0.1059	4.7573	5.5 ± 4.6
S4	9	1	174	0.0090	1.5747	3.2 ± 3.4
S5	7	1	241	0.0152	3.6515	0.7 ± 0.7
S6	17	68	1337	0.6285	12.3567	6.4 ± 2.9
S7	20	44	1021	0.3870	8.9798	7.7 ± 3.5
S8	15	0	801	0.0000	7.2423	-
S9	6	0	716	0.0000	12.7857	-
S10	8	16	479	0.2968	8.8868	5.3 ± 2.7
S11	1	0	20	0.0000	0.7813	-
S12	9	0	469	0.0000	6.3723	-
S13	34	23	6407	0.0785	21.8594	0.5 ± 0.1
S14	8	0	1270	0.0000	16.5796	-
S15	19	0	816	0.0000	3.3306	-
S16	50	1	654	0.0014	0.9160	0.3 ± 0.3
S17	95	9	2031	0.0079	1.7912	1.3 ± 1.3
S18	2	3	136	0.2206	2.2794	16.1 ± 9.7
S19	6	45	137	0.7500	2.2833	31 ± 17
S20	7	0	571	0.0000	8.9921	-
S21	6	0	299	0.0000	6.4440	-
S22	50	11	2911	0.0246	6.5036	0.7 ± 0.6

775